

# Efficient Optical Amplification in the Nanosecond Regime from Formamidinium Lead Iodide Nanocrystals

*Paris Papagiorgis<sup>†</sup>, Andreas Manoli<sup>†</sup>, Loredana Protesescu<sup>‡,#</sup>, Charis Achilleos<sup>†</sup>, Miltiadis  
Violaris<sup>†</sup>, Konstantinos Nicolaidis<sup>⊥</sup>, Theodosis Trypiniotis<sup>⊥</sup>, Maryna I. Bodnarchuk<sup>#</sup>, Maksym  
V. Kovalenko<sup>‡,#</sup>, Andreas Othonos<sup>||</sup> and Grigorios Itskos<sup>†,\*</sup>*

<sup>†</sup>Department of Physics, Experimental Condensed Matter Physics Laboratory, University of  
Cyprus, Nicosia 1678, Cyprus

<sup>‡</sup>Institute of Inorganic Chemistry, Department of Chemistry and Applied Biosciences, ETH  
Zürich, CH-8093 Zürich, Switzerland

<sup>#</sup>Laboratory for Thin Films and Photovoltaics, Empa – Swiss Federal Laboratories for Materials  
Science and Technology, Überlandstrasse 129, CH-8600 Dübendorf, Switzerland

<sup>⊥</sup>Department of Physics, University of Cyprus, Nicosia 1678, Cyprus

Department of Physics, Laboratory of Ultrafast Science, University of Cyprus, Nicosia 1678,  
Cyprus

\*itskos@ucy.ac.cy

KEYWORDS: perovskites, lead halides, nanocrystals, amplified spontaneous emission, optical gain, photoluminescence

Lead halide perovskites nanocrystals (NCs) were recently found to exhibit extraordinary optical amplification properties. The great majority of such studies, implemented ultrashort photon pulses in the femtosecond regime to initiate the stimulated emission process. Yet the realization of practical lasing applications based on such materials is crucially dependent on their ability to sustain optical amplification at significantly longer timescales, at which major losses associated with spontaneous emission and non-radiative recombination occur. Herein we demonstrate highly efficient amplified spontaneous emission (ASE) from closed-packed films of formamidinium lead iodide perovskite (FAPbI<sub>3</sub>) NCs under excitation in the nanosecond regime. Systematic optimization of the NCs processing and thermal treatment, yields solids that exhibit high ASE net modal gain up to 604 cm<sup>-1</sup> and nearly-temperature insensitive ASE thresholds with room temperature values as low as 140 μJ cm<sup>-2</sup>. The efficient optical amplification using excitation pulses comparable to the exciton lifetime combined with the excellent chemical durability and air stability of FAPbI<sub>3</sub> NCs renders them as outstanding gain media for continuous wave lasers in the red and near-infrared.

Colloidal semiconductor nanocrystals (NCs) are highly promising optical gain media combining the attributes of solution-processing with large transition oscillator strengths, size-tunable, broad optical gain spectra and potential for temperature-insensitive lasing operation arising from their three dimensional quantum confinement.<sup>1-2</sup> Since the first demonstration of the room-temperature optical gain in NC solids<sup>1</sup>, significant progress has been achieved based on synthetic and processing approaches allowing fabrication of densely packed NC films with reduced energetic and spatial disorder<sup>2</sup> combined with a better understanding of the exciton fine structure and nature of multicarrier interactions<sup>3-5</sup> and the implementation of appropriately engineered structures such as core-shell NCs that allow suppression of losses associated with surface and Auger recombination.<sup>6-8</sup> The breakthrough demonstration of continuous-wave lasing employing strain-engineered asymmetric NCs<sup>9</sup> and multishell-core NCs<sup>10</sup> to tailor the exciton fine structure and the spontaneous emission lifetime, respectively, follow the respective successes in colloidal quantum well gain media<sup>11</sup> and opens new avenues towards efficient colloidal nanocrystal lasers. The aforementioned progress has been based on metal chalcogenide semiconductor NCs, benefitted from decades of material development and structure optimization. The recent introduction of a new class of light emitting nanomaterials using lead halide perovskites of the type  $\text{APbX}_3$  with A being methylammonium, (MA), formamidinium, (FA), cesium (Cs) and X being Cl, Br, I and combination thereof<sup>12-16</sup> enables a further leap for breakthrough achievements in colloidal NC lasers. Extensive work on fully inorganic  $\text{CsPbX}_3$  NCs has already produced impressive results in amplified spontaneous emission (ASE) and lasing across the visible spectral region<sup>16-27</sup> with thresholds of just few  $\mu\text{J cm}^{-2}$  under femtosecond excitation, already surpassing those observed in  $\text{CdSe/ZnCdS}$  core-shell NCs<sup>7, 28</sup> and standing on par with record values reported in colloidal  $\text{CdSe/CdS}$  nanoplatelets<sup>11, 29-30</sup>. The good lasing properties indicate that losses in the optical amplification process due to Auger

recombination, that in Cs-based NCs appear to occur at similarly fast timescales to those in traditional metal chalcogenide NCs<sup>31-32</sup> and the retarded buildup of the stimulated emission due to slow thermalization of hot carriers<sup>33-35</sup> are well counterbalanced by the suppressed non-radiative recombination rising from the defect-tolerant electronic structure of perovskites.<sup>36-38</sup> Despite the successes, majorly based on all-inorganic perovskite NCs, the ambient thermodynamic and chemical instability of CsPbI<sub>3</sub> thin films and crystallites<sup>39-40</sup> renders such materials not suitable for light emitting applications in the red. The recent facile synthesis of robust formamidinium lead iodide perovskite (FAPbI<sub>3</sub>) NCs<sup>14, 41</sup> appears to largely circumvent the problem. Such NCs were found to exhibit outstanding optical properties with high quantum yields above 70%<sup>14</sup> and low ASE threshold under femtosecond excitation, down to 7.5  $\mu\text{J cm}^{-2}$ <sup>14</sup> combined with a significantly higher crystal chemical durability compared to the Cs-based counterparts in the red and near infrared region. Furthermore a recent report by Fang et al.<sup>42</sup>, provides evidence of significantly longer biexciton lifetimes compared to Cs-based NCs, making them highly suitable candidates for continuous wave lasing applications.

Motivated by the potential of such emitters we report here on a comprehensive study of the ASE properties of closed-packed FAPbI<sub>3</sub> NC films under excitation in the nanosecond regime. By controlling the processing, purification and thermal treatment of the NC films, we can produce two types of films containing isolated and partly sintered NCs, yielding distinct emission/ASE characteristics. ASE from isolated NCs was found to show high net modal gain up to 604  $\text{cm}^{-1}$  and only weakly temperature sensitive ASE thresholds with room temperature values down to 140  $\mu\text{J cm}^{-2}$ , a record low for ns-excited ASE in colloidal NCs. On the other hand, impressive but overall lower values of room temperature optical gain and ASE threshold values up/down to 502  $\text{cm}^{-1}$ /335  $\mu\text{J cm}^{-2}$  were found in films containing sintered NCs, combined with a significantly

stronger dependence of the ASE on sample temperature. Tuning of the purification, processing and thermal annealing parameters allow us to switch from the more quantum dot-like to the more sintered, bulk-like ASE behavior through intermediate film phases, in which both types of modes via the appearance of double ASE peaks are evidenced.

## Results and Discussion

### Distinguishing two types of FAPbI<sub>3</sub> NC solids

Our investigations employ as-synthesized FAPbI<sub>3</sub> NCs with cubic shape and average size of ~10 nm, estimated from the TEM image of **Figure 1(a)** and the Gaussian fitted NC size-histogram of **Suppl. Figure 1**. The optical properties of the NCs dispersed in toluene are displayed in **Figure 1(b)**, yielding energy gaps in the 1.64-1.62 eV range and bright photoluminescence (PL) peaked at 1.6-1.58 eV.

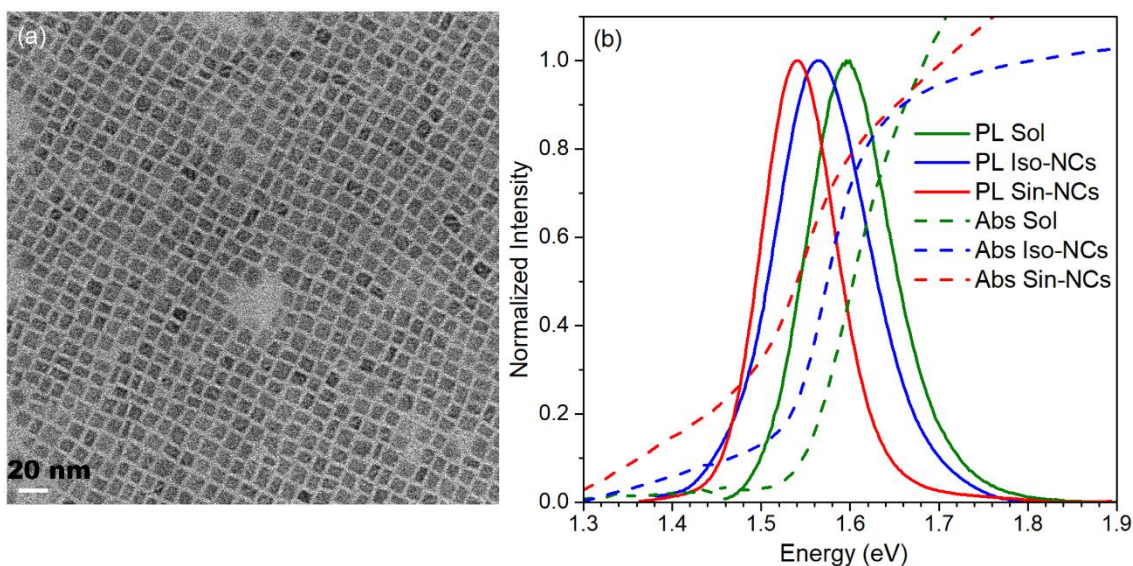


**Figure 1.** (a) TEM image of the studied, cubic FAPbI<sub>3</sub> NCs (b) Normalized absorbance and PL spectra from FAPbI<sub>3</sub> NCs dispersed in toluene (Sol) and films processed out of the NC solution with optical characteristics attributed to isolated (iso-NC) and partly sintered (sin-NC) nanocrystals.

As spun, drop-casted or spin-coated films, subjected to purification using non-polar solvents (see Materials and Methods section) were found to exhibit sharp band edges with band-gaps and PL peaks slightly red-shifted i.e. by  $\sim 25\text{-}35$  meV compared to the respective features of the as-synthesized NC colloids as observed in **Figure 1(b)**. The photophysical behavior, as further supported by additional experimental evidence below in the text, is consistent with solids in which the NC surface retains a considerable amount of the oleic acid ligands, preventing NC aggregation and preserving the integrity of individual NCs, termed “isolated NCs” (iso-NCs) films for the rest of the manuscript. On the other hand, films deposited via dip-coating or spin-coating that have been treated using a processing protocol employing a polar solvent rinsing, exhibited consistently larger bathochromic absorption and PL shifts up to 60 meV compared to the respected values in colloids, with less well-defined band-edges and pronounced band-tail contribution. It appears that treatment with a polar solvent results in partial detachment of the weakly bound ligands from the surface allowing the NCs to pack and partly merge forming “sintered NCs” (sin-NCs) films. The observation is supported by recent surface chemistry studies on perovskite NCs which demonstrate the highly dynamic nature of surface ligand binding, resulting in ligands loss during purification steps, especially when such processes involve polar solvents.<sup>43,44</sup> The ligand loss appears further pronounced in dip-coated films due to the elevated temperature used during the film drying step.

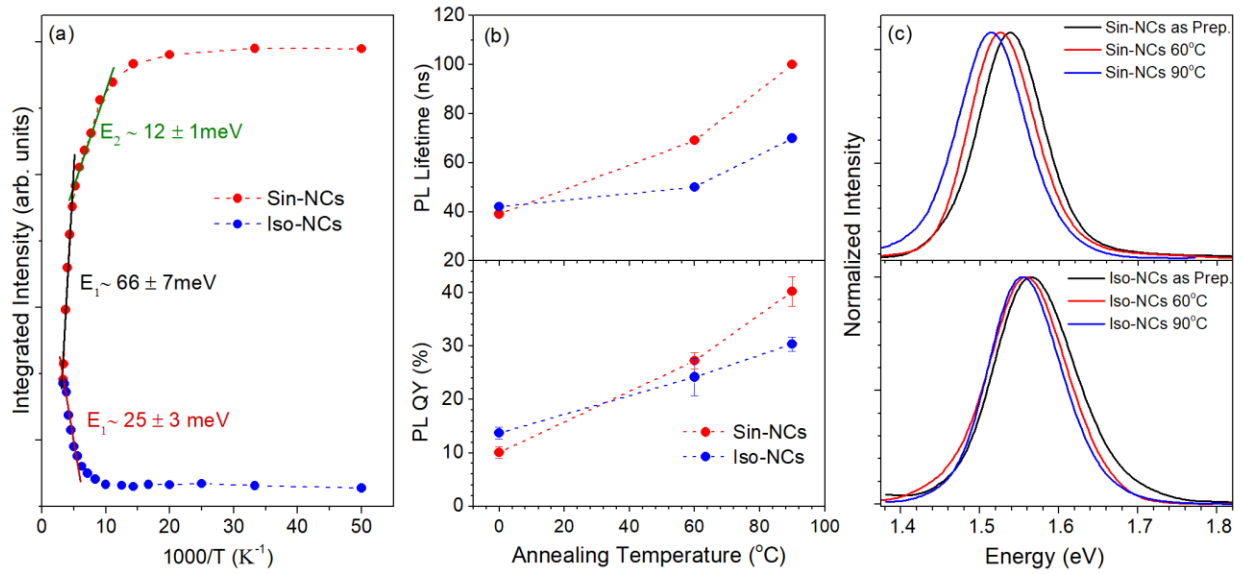


**Figure 2.** (a) Representative Arrhenius plots of the two types of NC films. (b) Impact of post-deposition thermal annealing on the average PL lifetimes (top) and PL QY (bottom) of the two film types. (c) PL shifts upon thermal annealing from iso- and sin-NC films.

Such a hypothesis is further supported by the two distinct temperature-dependent PL behaviors of the two film types, represented in the Arrhenius plots of **Figure 2(a)** and the raw data of **Suppl. Figure 2(a)** and **2(b)** with the PL intensity of the necked (isolated) NC films, quenching (growing) as temperature is raised. Both NC solids were found to exhibit a characteristic PL peak dependence with temperature illustrated by **Suppl. Figures 2(c)** and **2(d)**, that has been previously observed in bulk-<sup>45</sup> and nano-crystal<sup>42</sup> films of  $\text{FAPbI}_3$  and convincingly assigned to a crystal structure transition from a tetragonal to an orthorhombic phase. The almost identical and fully reversible temperature evolution of the PL peak in all films studied, can exclude the presence of different perovskite crystal phases as the origin of the two distinct optical behaviors observed. For the sin-NC films, analysis of the Arrhenius plots reveal an activation-type of PL quenching yielding typically two linear regions with respected activation energies in the range of 10-14 meV and 60-90 meV. The former quenching process is attributed to exciton-LO-phonon

interactions, based on the measured 11.5 meV value of the LO phonon of FAPbI<sub>3</sub> <sup>46</sup> while the latter mechanism is most probably related to exciton thermal escape from the NCs as the respective activation energy matches the NC confinement energy i.e. the separation of the NCs absorption edge from the bulk FAPbI<sub>3</sub> gap of ~1.48 eV.<sup>47</sup> The aforementioned model is also consistent with the temperature-activated quenching of the PL lifetime, presented in **Suppl. Figure 3**. On the other hand, the anomalous growth of the intensity and the PL lifetime (**Suppl. Figure 4(a)** and **4(b)**) with temperature in the iso-NC films appear consistent with a thermally induced exciton detrapping process. The fluence-insensitivity of the PL transients (**Suppl. Figure 4(c)**) and the strictly linear variation of the zero-delay PL intensity **Suppl. Figure 4(d)** across the power density range used in our PL experiments, excludes the possibility that the anomalous temperature variation originates in formation and recombination of multi- or charged-exciton species. On the other hand the exciton detrapping model has also been used by Fang et al.<sup>42</sup> in FAPbI<sub>3</sub> NC solids with the authors attributing the trapping to a surface dark exciton state. In our study, evidence by low temperature PLE experiments displayed in **Suppl. Figure 5**, indicate the presence of absorbing species in the gently-purified iso-NC films related to unreacted PbI<sub>x</sub> precursors. PbI<sub>2</sub>-rich regions were found to influence the charge carrier lifetimes and PL emission yield in hybrid perovskites.<sup>48</sup> It is thus probable that such defects are responsible for the efficient low temperature trapping of excitons in the iso-NC films. From the Arrhenius plots, a distribution of activation energies in the 10-30 meV range can be extracted that provide an estimate of the exciton localization energies in such PbI<sub>x</sub>-related defects.

The thorough cleaning of the sin-NC films appears to largely remove such defects, yet both their room temperature emission lifetime and the quantum yield (QY) does not concomitantly increase compared to the less washed iso-NC films, that were typically found to exhibit slightly larger room temperature PL lifetimes and QYs. It is plausible that the beneficial effect of washing off



byproducts of synthesis is counterbalanced by emission quenching introduced upon colloidal NC necking.<sup>49</sup> Thermal annealing, that appears as a necessary post-deposition processing step to improve the solid-state mesoscale morphology and achieve high performance optical amplification in the FAPbI<sub>3</sub> NCs, differentiates even further the optical behavior of the two types of films. The impact of annealing becomes pronounced above 60 °C and is optimized for both types of NCs at 90 °C, as witnessed by the monotonic enhancement of the emission intensity and lifetime displayed in **Figure 2(b)** and **Suppl. Figure 6**. It becomes though evident that the thermal treatment has a much stronger beneficial effect for the sin-NC films, i.e. for the representative example of **Figure 2(b)** the PL lifetime/QY in the sin-NC films increases by a factor of 2.5/4 compared to respective improvements by a factor of 1.7/2.2 in the iso-NC film. Furthermore, annealing results in a significantly larger bathochromic emission shift in the sin-NC films, lowering their PL peak energy down to ~1.51 eV upon annealing at 90 °C, approaching the bulk FAPbI<sub>3</sub> gap of 1.48 eV as observed in **Figure 2(c)**. The loss of confinement is consistent with a more pronounced merging of the NCs induced by the thermal treatment in such films. The optical data trends are further supported by microscopy measurements presented in **Figure 3** and **Suppl. Figure 7** that probe the effect of polar solvent washing and post-deposition annealing on the microstructure of iso- and sin-NC films. For sin-NCs, such morphological changes are pronounced and are both visible in TEM and AFM images. Thermal annealing at 85<sup>0</sup>C for 5 min is sufficient to activate the NC aggregation process, resulting in sintering of ~30% of the imaged NCs as seen in the pre- and post-annealing TEM images of sin-NCs in **Figures 3(a)** and **3(b)**, respectively. Furthermore AFM images of non-annealed sin-NC films, subjected to a polar washing cycle, indicate that even before thermal treatment, NC merging is observed as seen in **Suppl. Figures 7(a)** and **7(c)**. Upon annealing, NC merging becomes significantly more pronounced, producing larger, one-dimensional structures, evident in

**Suppl. Figures 7(b) and 7(d).** In a fraction of the studied sin-NC films, the sintering is so extensive that nanowires with length of tens of microns and submicron width and height i.e. width of  $\sim 400\text{-}600$  nm and height of  $\sim 100\text{-}150$  nm for the representative example of **Figure 3(d)**, are formed. On the other hand no consistent evidence of the formation of large nanostructure assemblies exists in thermally treated iso-NC films as seen in **Figure 3(c)**, which combined with the negligible red-shift of their PL spectra upon annealing displayed in **Figure 2(c)** indicates that the  $\text{FAPbI}_3$  nanocrystals in such films remain largely in the as-grown, confined state.

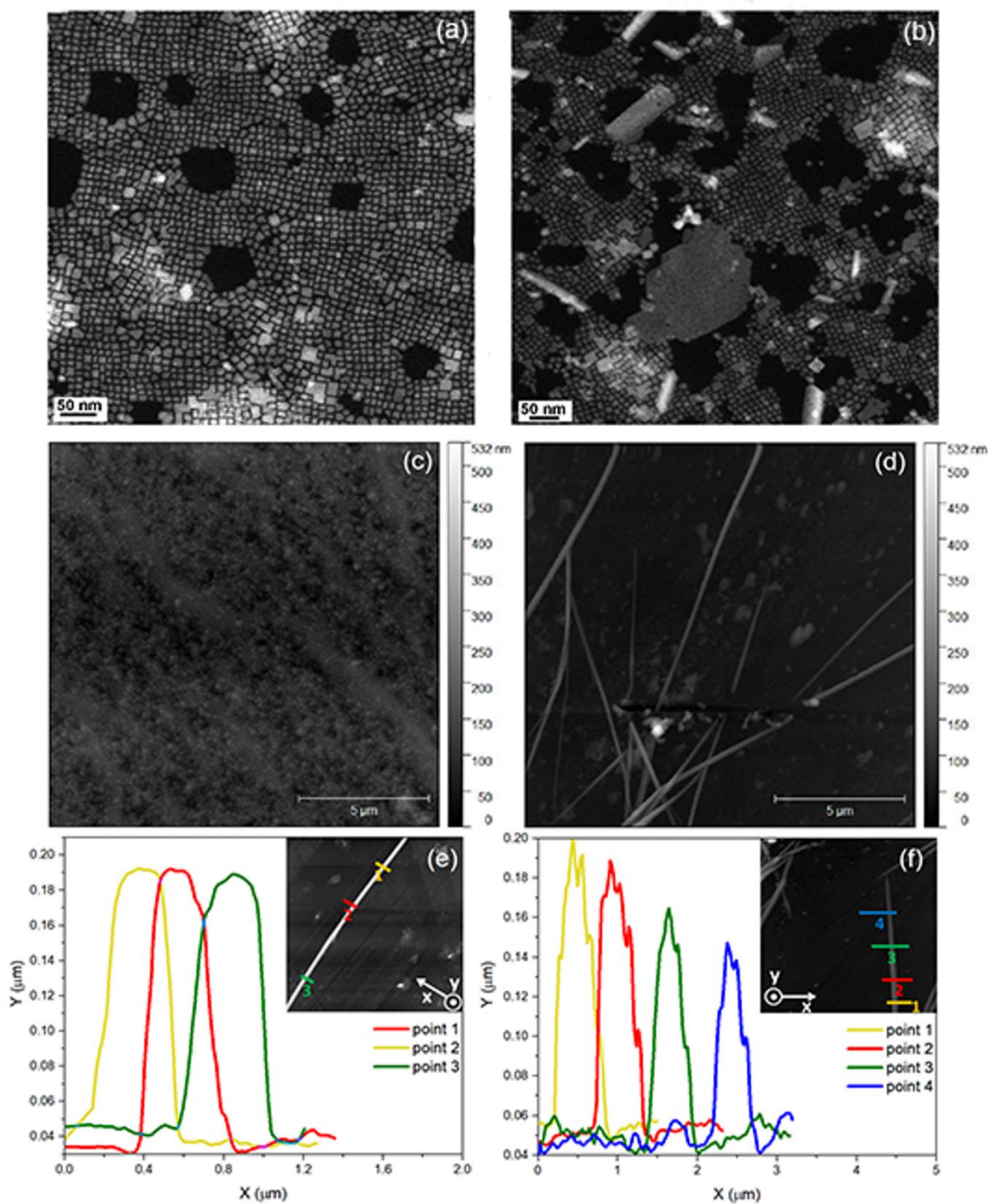


**Figure 3:** Transmission electron microscopy images of polar-washed NCs on a TEM grid **(a)** before and **(b)** after thermal annealing for 5 min at 85° C. Atomic force microscopy images yielding the surface morphology of **(c)** an iso-NC film and **(d)** a sin-NC film, both annealed at 90° C for 30 min. **(e,f)** AFM images of nanowires formed in films of sintered NCs imposed to the

aforementioned thermal treatment. From the graphs, estimates of the width (x) and height (y) of the nanowires across different cross sections within the wires length, are provided.

### **Room-temperature amplified spontaneous emission under nanosecond excitation**

Both types of NC films exhibit emission narrowing and threshold type behaviour for high enough excitation fluences that signature the appearance of ASE. To achieve room-temperature ASE, the films had to be subjected to an annealing step applied during or subsequent to deposition. The influence of the thermal treatment on the optical gain characteristics is elaborated later in the text. Films containing isolated NCs, exhibit ASE peaks in the vicinity of the respective PL maximum, in the range of 1.55-1.57 eV as observed in **Figure 4(a)**. On the other hand films with partially necked NCs, exhibit consistently ASE on the lower energy wing of the PL, as displayed in **Figure 5(a)**, lying at or slightly above the  $\text{FAPbI}_3$  gap, i.e. in the 1.48-1.52 eV range, confirming the confinement loss of the NCs in such case.

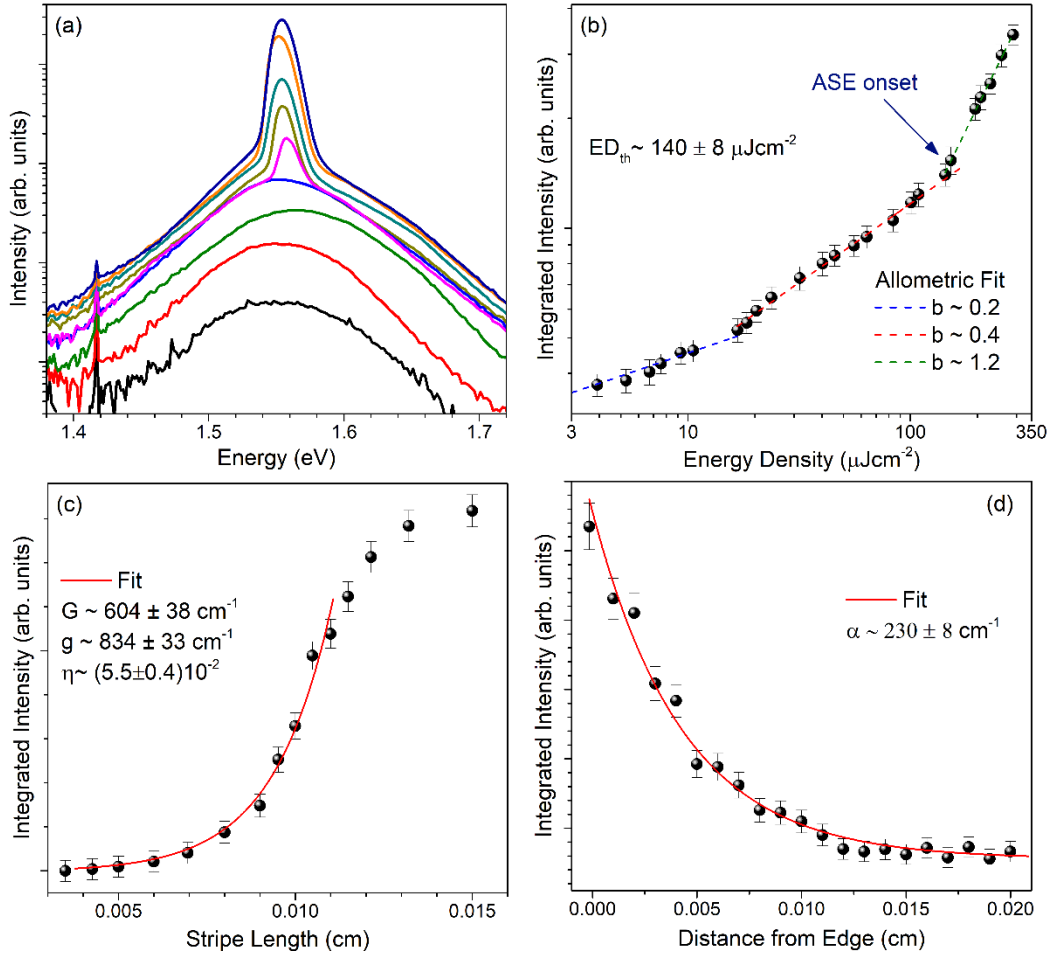


**Figure 4:** ASE excited from an iso-NC drop-casted film thermal-treated subsequent to film deposition at  $90^\circ \text{C}$ : **(a)** ASE spectra at different excitation fluences. The y-axis is displayed in logarithmic scale. **(b)** Integrated emission versus excitation energy density. Allometric fits of the data with the respective fitted exponents are also displayed. The ASE onset is clearly defined by the sub- to super-linear change of slope **(c)** Integrated intensity versus stripe length obtained using the variable stripe length geometry. The fit using equation (3) and the extracted optical gain parameters are also displayed. **(d)** Integrated intensity versus stripe distance from the sample edge, for a constant stripe length. The method allows the estimation of the ASE optical loss using the Beer-Lambert type of fit of equation (4)

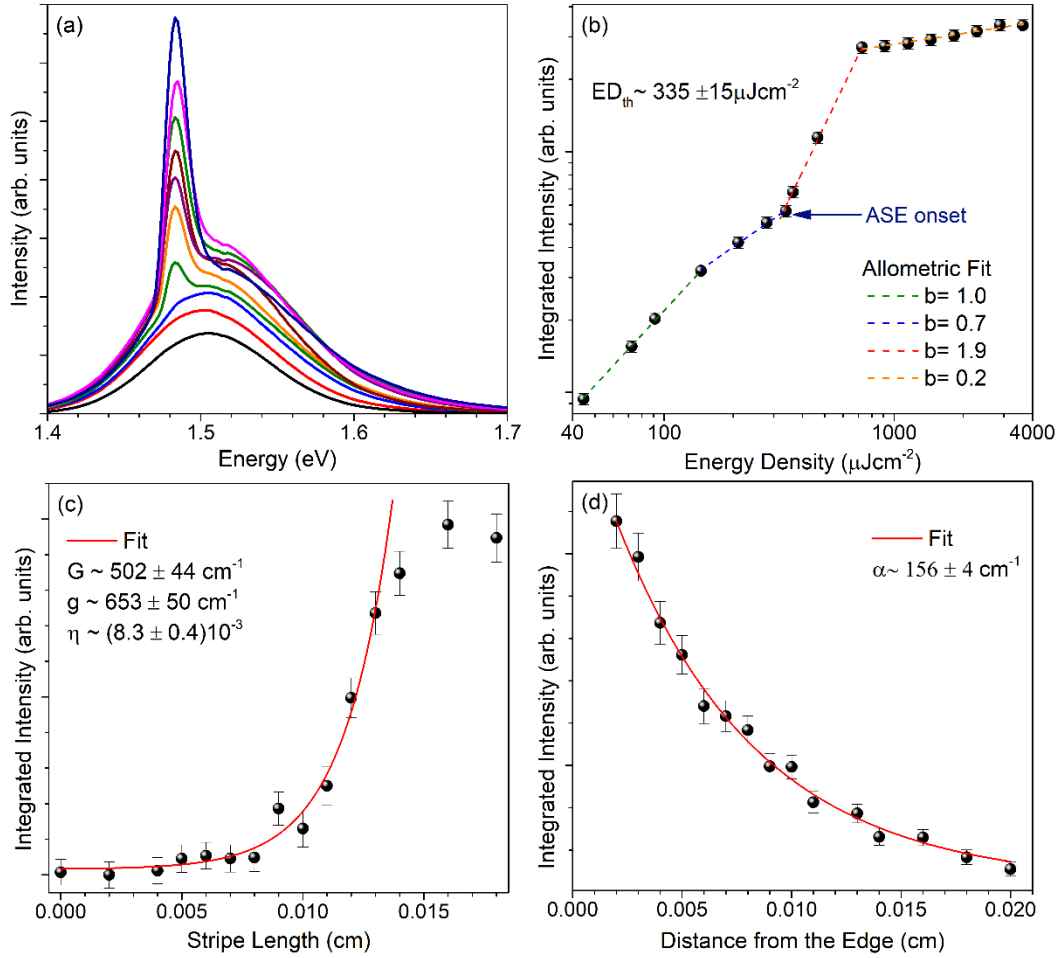


**Figure 5:** ASE from a sin-NC drop-coated film imposed to post-deposition annealing at  $90^\circ\text{C}$ : **(a)** ASE spectra at different excitation energies. **(b)** Integrated emission versus excitation energy density along with allometric fits of the data. The ASE threshold is again defined by the sub- to super-linear change of slope **(c)** Integrated intensity versus stripe length obtained using the variable stripe length geometry along with fits and extracted optical gain parameters. **(d)** Integrated intensity versus stripe distance from the sample edge, used for the estimation of the ASE losses.

The ASE threshold is extracted from the excitation dependence of the integrated emission, displayed in **Figures 4(b)/5(b)** for iso-/sin-NC films respectively. The former exhibit consistently lower ASE thresholds down to  $140 \mu\text{J cm}^{-2}$  and typical values in the range of  $\sim 150$ -

300  $\mu\text{J cm}^{-2}$  compared to a minimum threshold of 335  $\mu\text{J cm}^{-2}$  and mean values in the 350-450  $\mu\text{J cm}^{-2}$  range for the bulk-like NC films. The threshold reported in the isolated NC solids appears to constitute a record low for nanosecond-excited ASE from colloidal NC films. At the same time, recent studies on ns-excited ASE in films of FAPbI<sub>3</sub> bulk crystals<sup>50</sup> set an even lower, by as much as a factor of 7, threshold bound, paving the way towards further optimization of the quasi-continuous optical amplification properties of NCs based on the FAPbI<sub>3</sub> perovskite.

The ASE linewidth for the isolated NCs was measured in the range of 18-26 meV, being typically larger than the respective linewidth in bulk-like films in which values as low as 10 meV were obtained. Yakunin et al.<sup>17</sup> reported on an inverse relationship between the ASE linewidth and the ASE threshold in CsPbBr<sub>3</sub> perovskite NCs, as samples with low thresholds support a larger optical gain bandwidth. Such an explanation appears consistent with our data, with films containing mostly isolated NCs yielding lower ASE thresholds and larger FWHMs compared to the respective parameters of sintered NCs, indicative of a larger ASE bandwidth in the former solids.

The efficiency of optical amplification is quantitatively accounted by the net modal gain  $G$ , measured via the variable stripe length (VSL) method<sup>51</sup> using sample excitation via a light stripe with adjustable length and detection of the edge-emitted ASE as a function of stripe length, as illustrated in **Suppl. Figure 8**. The VSL results are displayed in **Figures 4(c)/5(c)** for iso/sin-NC films, respectively. The growth of the integrated intensity from the onset of ASE and through the excitation regime where no saturation effects are visible, can be modelled by the following rate equation<sup>52</sup>:

$$\frac{dI(\lambda, x)}{dx} = g(\lambda)I(\lambda, x) - a(\lambda)I(\lambda, x) + ng(\lambda) \quad (1)$$

Where  $g$  is the optical gain,  $\alpha$  is the optical loss coefficient and  $n$  is a parameter proportional to the spontaneous emission rate and to a geometrical factor dependent on the sample dimensions. The optical gain  $g$ , loss  $\alpha$  and net modal gain  $G$  parameters are connected via the relationship:

$$G(\lambda) = g(\lambda) - \alpha(\lambda) \quad (2)$$

Integration of equation (1), using the boundary condition  $I(\lambda, x=0) = 0$ , yields the following fitting model of the experimental data:

$$I(\lambda, x) = \frac{A(\lambda)}{G(\lambda)} (e^{Gx} - 1) \quad (3)$$

Where  $A(\lambda) = n g(\lambda)$ . Model (3) produces good fits of the experimental data, as seen in **Figures 4(c)/5(c)** and yields the parameters  $G(\lambda)$  and  $A(\lambda)$ , with values of net modal gain as high as 604  $\text{cm}^{-1}$  and 502  $\text{cm}^{-1}$  for NC-like and bulk-like films, respectively. The absorption and scattering losses defining the coefficient  $\alpha$  can be estimated using a variation of the VSL method, in which the excited beam is translated away from the sample edge, while keeping the stripe length fixed to a value just above the ASE onset. The loss  $\alpha$  can then be extracted by fits of the following Beer-Lambert law function, as observed in **Figures 4(d)/5(d)** for iso/sin-NC films, respectively:

$$I(\lambda, d) = I(\lambda, 0) e^{-\alpha d} \quad (4)$$

Where  $I(\lambda, 0)$  the ASE intensity obtained with the pumping stripe at the edge of the film, and  $d$  the distance by which the stripe is translated away from the edge. The optical gain  $g$  and the parameter  $n$  can also be obtained from the fit extracted values of  $G$  and  $A$  using the relation (2) and the equation defining the quantity  $A$ . All extracted optical gain parameters are displayed in Figures 2 and 3 for the best performing iso/sin-NC films, respectively.

High net modal gain and low ASE threshold values are observed only after NC annealing during or subsequent to solid state deposition. For films containing partly merged FAPbI<sub>3</sub> NCs, thermal treatment at a minimum temperature of 60 °C appears as a prerequisite step to achieve ASE. For iso-NCs films, ASE was also observed in a small fraction of non-annealed films albeit at the



expense of higher fluence thresholds. The impact of post-deposition annealing on a film with confined NCs is displayed in **Figure 6**. Baking up to 60 °C increases the net modal gain by ~1.5 times, mainly via reducing scattering losses by a factor of ~2.3. A further optimization of the net modal gain up to an annealing temperature of 90 °C is observed, due to a modest increase of the optical gain by ~20%. The highly favourable impact of annealing on ASE is consistent with the strong enhancement on the intensity and dynamics of the luminescence discussed in the previous section of the manuscript.

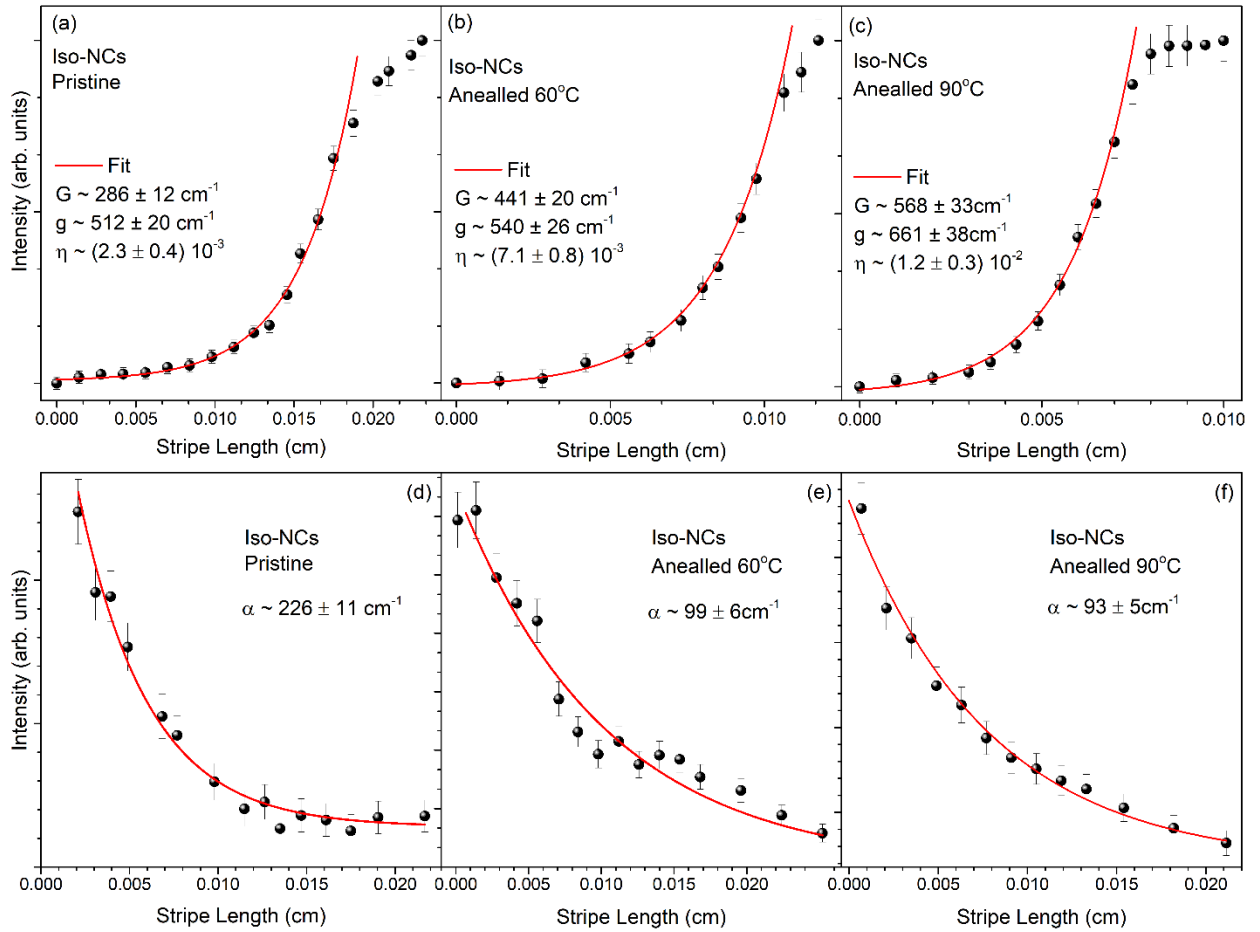


**Figure 6:** Impact of thermal annealing on: (a,b,c) the gain characteristics and (d,e,f) the optical losses, of the same film, containing isolated FAPbI<sub>3</sub> NCs.

## Temperature dependence of the amplified spontaneous emission

**Figures 7(a) and (b)** show representative examples of the temperature variation of the ASE threshold for iso- and sin-NC films respectively, imposed to post-fabrication annealing. For isolated NCs, the threshold appears to strongly increase with temperature from 40 to 290 K by a factor of  $\sim 5$  and  $\sim 3$  for the non-annealed and the annealed at 60 °C film, respectively. On the other hand an almost temperature-insensitive onset of ASE is observed for the film annealed at the optimum temperature of 90 °C with an overall threshold variation of less than 30% across the temperature range probed. The origin of the temperature-insensitive threshold, observed in a significant fraction of the iso-NC films studied, is not fully resolved. We hypothesize that it may be the result of two competing mechanisms, namely thermally-activated exciton detrapping evidenced by the anomalous growth of the emission intensity with temperature discussed earlier, with quenching mechanisms that antagonize the population inversion such as non-radiative recombination as temperature increases. In films containing mostly necked NCs, a strong growth of the ASE threshold with temperature is observed for both pristine and thermally-treated samples. An interesting observation is that in a subset of the sintered NC films, two ASE peaks emerge at low temperatures, as illustrated in the example of **Figure 7(c)** for a film annealed subsequent to deposition at 60 °C. The high energy peak 1 appears energetically coincident with the PL maximum while the low energy peak 2 emerges in the long wavelength PL tail, red-shifted by 20-45 meV in respect to peak 1 and the PL maximum as displayed in **Suppl. Figure 9**. The two ASE features match the energetic position of the respective ASE peaks found in the iso- and sin-NC films, as illustrated in **Figures 4 (b)/5(b)**, respectively. The dual ASE is then attributed to optical gain from a coexistence of phases within the film, with areas of isolated NCs and domains in which merged NCs dominate, responsible for the peaks 1 and 2, respectively. When the film is imposed to an additional annealing step to 90 °C, ASE peak 1 due to isolated

NCs vanishes and the ASE threshold assumes a temperature variation resembling the ASE peak 2, as the pronounced thermal treatment results in complete sintering of the perovskite nanocrystals.

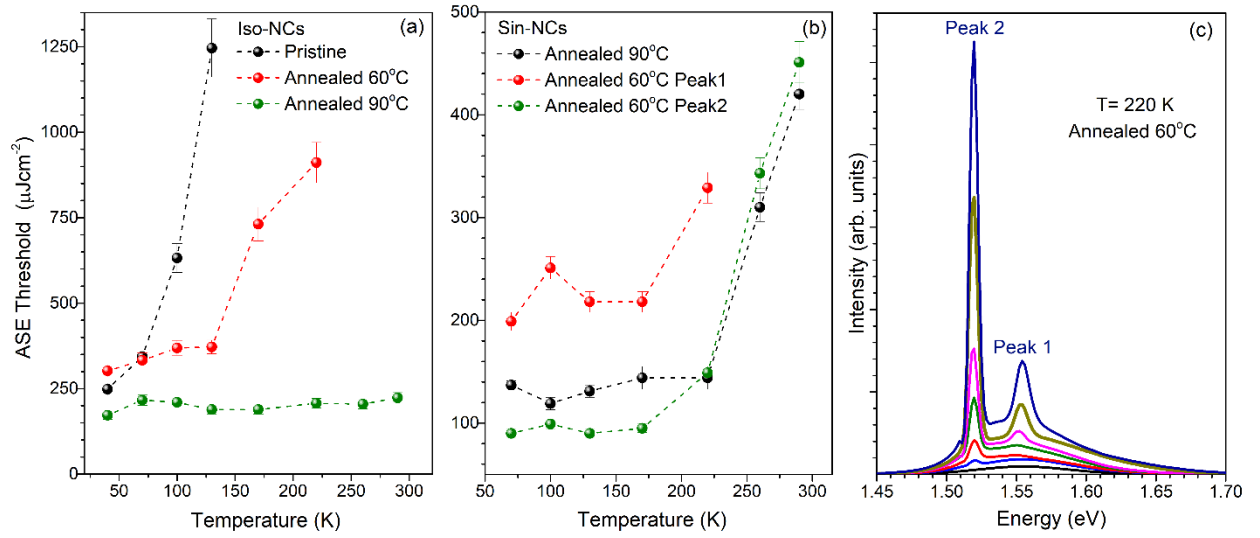


**Figure 7:** Temperature dependence of the ASE threshold for a film containing intact NCs, annealed at different temperatures subsequent to film deposition. **(b)** Evolution of the ASE threshold with temperature for a film containing necked NCs. When annealed at 60 °C, the film sustains two ASE peaks. (c) The emergence of the dual ASE at 220 K from the latter film.

The temperature variation of the ASE linewidths from the two categories of NC solids is shown in the graphs of **Suppl. Figure 10**. As discussed earlier, films with confined NCs exhibit typically broader ASE peaks compared to those of sintered NCs, attributed to an increased optical gain bandwidth. The bandwidth appears to be further increased by thermal annealing up to 90 °C, consistent with the concomitant decrease in the ASE threshold for both type of films upon such thermal treatment. For both iso- and sin-NCs, the ASE FWHM overall increases with temperature, assuming a similar pattern to that of the luminescence linewidth growth, however

ASE/PL narrowing is also observed in the temperature range of 50-130 K, where NC crystal structure phase transitions occur, as discussed earlier in the text.

## Conclusions

We report on the photophysical and optical gain properties of closed-packed films of FAPbI<sub>3</sub> NCs under excitation in the nanosecond regime. The impact of purification, processing and post-deposition thermal treatments on the integrity and confined state of the NCs is demonstrated, resulting in two distinct emission and optical amplification behaviors attributed to films with isolated and partly sintered NCs. The quantum dot-like films exhibit outstanding room-temperature ASE characteristics under nanosecond excitation, with low ASE threshold down to 140  $\mu\text{J cm}^{-2}$  and high net modal gain up to 604  $\text{cm}^{-1}$  which combined with the material robustness in ambient conditions, makes them excellent candidates for applications in lasing applications.

## Materials and Methods

Chemicals: Formamidinium acetate (FA-acetate, Aldrich, 99%), lead (II) iodide (Aldrich, 99%), lead (II) acetate (Aldrich,  $\geq 99.99\%$ ), octadecene (ODE, Aldrich, 90%), mesitylene (MS, Sigma-Aldrich, 98%), oleic acid (OA, Aldrich, 90%), Oleylamine (OLA, Acros Organics, 80-90% or STREM, 95%), HI (ABCR, 57 % aqueous solution with stabilizer), hexamethyldisilazane (Aldrich, 99%), toluene (Aldrich, 99.8 %), hexane (Aldrich, 98.5 %), ethanol (Aldrich, absolute,  $> 99.8\%$ ), acetonitrile (Sigma-Aldrich,  $\geq 99.5\%$ ), methyl acetate (ABCR, 99%), diethyl ether (Sigma-Aldrich,  $\geq 99.8\%$ )

**Synthesis:** The FAPbI<sub>3</sub> NCs were prepared using the following two synthetic methodologies, according to published procedures (14). It is noted that the two synthetic methods result in nanocrystals with identical structural and photophysical properties, as elaborated in reference (14).

**Method 1.** PbI<sub>2</sub> (0.172 g, 0.374 mmol) and MS (10 mL) were added to a 50-mL round-bottom flask, dried for 1 h at 120 °C and mixed with OA (2 mL, vacuum-dried at 120 °C) and OLA (1 mL, vacuum-dried at 120 °C). When the PbI<sub>2</sub> was fully dissolved and the mixture was cooled to 80 °C, the preheated FA-oleate precursor (4 mL, prepared in advance as described below) was injected. After 60 s of stirring, the solution was cooled to RT in a water bath. *Preparation of FA-oleate precursors:* FA-acetate (0.521 g, 5 mmol), 16 mL of ODE (vacuum-dried at 120 °C) and OA (4 mL) were added to a 50-mL round-bottom flask. The mixture was degassed for 10 min at RT and then heated under nitrogen to 130 °C, which yielded a clear solution. Next, the clear solution was dried for 30 min at 50 °C under vacuum. FA-oleate was heated to 100 °C before use because it often precipitates when cooled to RT.

**Method 2.** In a 25 mL three-necked flask lead (II) acetate (76.0 mg, 0.234 mmol) and formamidinium acetate (78.0 mg, 0.75 mmol) were dissolved in ODE (8.0 mL) and OA (2.0 mL). The solution was dried at room temperature for 5 min and then at 80 °C for 30 min. At 80 °C a solution of oleylammonium iodide (237 mg, 0.6 mmol) in toluene (2.0 mL) was injected under N<sub>2</sub>. The reaction was cooled to room temperature immediately with the water bath. *Preparation of oleylammonium iodide:* 60 mL acetonitrile and 38.4 mL oleylamine (0.11 mol) were combined and heated to 50-60 °C. At this temperature 25 mL HI (0.19 mol) was added. Solution was stirred overnight. Next, the solution was dried under vacuum, and the obtained product was

recrystallized multiple times from diethyl ether and then isolated as a white powder by vacuum-drying at 80°C

#### Films processing:

(a) Processing and deposition of iso-NC films: The crude solution from the synthesis was centrifuged for 5 min at 12100 rpm and the supernatant solution was discarded. The precipitate was redispersed in 400  $\mu$ L hexane and centrifuged again. The precipitate was suspended in 6 mL of toluene and centrifuged at 4400 rpm for 3 min. Next, the precipitate was discarded and the supernatant solution was filtered through a 0.45  $\mu$ m PTFE filter. Subsequently the solution was concentrated under vacuum until the concentration of 40 mg/mL was reached. Immediately after this step, 20-30  $\mu$ L from the concentrated solution were spin-coated or dropped casted on a glass substrate pre-cleaned with acetone and ethanol and pre-treated with hexamethyldisilazane.

b) Processing and deposition of sin-NC films: The crude solution from the synthesis was centrifuged for 5 min at 12100 rpm and the supernatant solution was discarded. The precipitate was dissolved in toluene (1.0 mL) and methyl acetate (250  $\mu$ L) was added and the solution was centrifuged again at 12100 rpm for 7 min. The supernatant was discarded whereas the precipitate was dissolved in 4 mL octane and filtered through a 0.45  $\mu$ m PTFE filter. Films were deposited out of spin-coating using the same procedure with that described above for the iso-NC films or via dip-coating using one of the two following methods:

a) Films were prepared on PEDOT:PSS treated glass slides by withdrawing the slide from octane solution of FAPbI<sub>3</sub> NCs at a rate of 10 mm/min. The dipping and constant-rate withdrawing was repeated 42 times to yield thick films.

b) 1 mL of FAPbI<sub>3</sub> NCs in octane was dried and precipitate. It was then redispersed in 3 mL toluene. Films were prepared on PEDOT:PSS treated glass slides by withdrawing the slide from the toluene solution at a rate of 10 mm/min and then baking the slide inside an oven at 82 °C for 3 min. Next, the slide was cooled to room temperature and immersed in pure toluene, withdrew from it again with the rate 10mm/min and dried at room temperature. The sequence was repeated 40 times to yield thick films.

The aforementioned three deposition methods (spin-coating, dip-coating, drop-casting) resulted in films with thicknesses widely varied in the ~150-500 nm range, measured by AFM microscopy. The optimum ASE characteristics have been obtained with dip-coated and drop-casted films with thicknesses in the range of ~250-350 nm.

#### Optical Spectroscopy:

Absorbance of films was recorded with a Perkin Elmer Lamda 1050 spectrophotometer covering the 200-3000 nm spectral range. Steady-state photoluminescence (PL) and amplified spontaneous emission experiments were carried out using a 0.75 m Acton750i Princeton spectrometer equipped with a 1024x256 pixels PIXIS charge-coupled device (CCD) camera with spectral response in the range of 300-900nm. The films were excited at 532 nm, using the second harmonic of a Quantel Brilliant Nd:YAG laser producing a 4 mm beam with pulse width of ~4 ns and repetition rate of 10 Hz. The energy density of the excitation beam was varied in the 1 – 4000  $\mu\text{J cm}^{-2}$  range using neutral density filters. ASE and PL emission were detected using both a side (stripe excitation spot) and a back-scattering (round excitation spot) geometry in our experiments. A small improvement in the ASE threshold was found in the side detection geometry. In the variable stripe length (VSL) experiments, a cylindrical lens ( $f \sim 200$  mm) was employed to convert the circular beam of the laser into a rectangular strip with dimensions of

~1.5 x 7.0 mm. The length of the strip was varied using a precision adjustable slit with micrometer sensitivity of 5  $\mu\text{m}$ . The VSL geometry is displayed in Suppl. Figure 6. Photoluminescence quantum yield (PL QY) was measured according to the method described by de Mello et al.<sup>53</sup> using a 4 inch integrating sphere (Edmund Optics) coupled to the aforementioned grating spectrometer via an optical fiber bundle. Temperature-dependent PL/ASE measurements in the 10-300 K range were carried out by placing the samples in the cold finger of a Janis CCS-150 closed-cycle refrigerator.

Time resolved photoluminescence (PL) was recorded on a FluoroLog FL3 Horiba Jobin Yvon spectrofluorimeter using a monochromator based time correlated single photon counting (TCSPC) method. The PL was excited by a 633 nm laser diode (DeltaDiode-633L) with a pulse width of ~80 ps respectively, operating at 100-250 KHz. The system exhibits a time resolution of ~50 ps after reconvolution with the instrument response function. The PL decays were obtained while monitoring the PL emission peak with a spectral bandwidth of ~2nm. The average transient PL lifetime  $\tau_{av}$  for TRPL decays was calculated from the relation:

$$\tau_{av} = \frac{\sum_i A_i \tau_i^2}{\sum_i A_i \tau_i}$$

where  $\tau_i$  are the decay times extracted from multi-exponential fits of the PL transients and  $A_i$  the corresponding decay amplitudes.

## ASSOCIATED CONTENT

### Supporting Information.

The following file is available free of charge. TEM nanocrystal histogram, PL spectra, PL



transients and ASE characteristics (energy position, linewidth) as a function of temperature, low temperature PLE data, AFM images, schematic and photographs of experimental setups (PDF)

## AUTHOR INFORMATION

### Corresponding Author

\*itskos@ucy.ac.cy

### Author Contributions

The manuscript was written through contributions of all authors. All authors have given approval to the final version of the manuscript.

## ACKNOWLEDGMENT

M.V. K. acknowledges financial support from the European Research Council under the European Union's Seventh Framework Program (Grant Agreement Nr. 306733, ERC Starting Grant “NANOSOLID”). M.B. acknowledges the Swiss National Science Foundation (SNF Ambizione Energy grant, Grant Nr. PZENP2\_154287).

## References

1. Klimov V. I.; Mikhailovsky A. A.; Xu S.; Malko A.; Hollingsworth J. A.; Leatherdale C. A.; Eisler H.-J.; Bawendi, M. G. Optical Gain and Stimulated Emission in Nanocrystal Quantum Dots. *Science*. **2000**, 290, 314–317.
2. Kovalenko M. V.; Manna L.; Cabot A.; Hens Z.; Talapin D.V.; Kagan C. R.; Klimov V. I.; Rogach A. L. Reiss P.; Miliron D. J.; Guyot-Sionnest P.; Konstantatos G.; Parak W. J.; Hyeon T.; Korgel B. A.; Murray C. B. Heiss W. Prospects of Nanoscience with Nanocrystals. *ACS Nano*. **2015**, 9, 1012.

3. Efros A. L.; Rosen M.; Kuno M.; Nirmal M.; Norris D. J. Bawendi M. Band-edge exciton in quantum dots of semiconductors with a degenerate valence band: dark and bright exciton states. *Phys. Rev. B*. **1996**, 54, 4843–4856.
4. Franceschetti A.; Fu H.; Wang L. W.; Zunger A. Many-body pseudopotential. *Phys. Rev. B*. **1999**, 60, 1819–1829.
5. Klimov V. I. Multicarrier interactions in semiconductor nanocrystals in relation to the phenomena of Auger recombination and carrier multiplication. *Annu. Rev. Condens. Matter Phys.* **2014**, 5, 285–316.
6. Klimov V. I.; Ivanov S. A.; Nanda J.; Achermann M.; Bezel I.; McGuire J. A.; Pirayattinski A. Single-exciton optical gain in semiconductor nanocrystals. **2007**, 447, 441–446.
7. Dang C.; Lee J.; Breen C.; Steckel J. S.; Coe-Sullivan S.; Nurmikko A. Red, green and blue lasing enabled by single-exciton gain in colloidal quantum dot films. *Nat. Nanotechnol.* **2012**, 7, 335–339.
8. Chen O.; Zhao J.; Chauhan V. P.; Cui J.; Wong C.; Harris D. K.; Wei H.; Han H.-S.; Fukumura D.; Jain R. K.; Bawendi M. G. Compact high-quality CdSe–CdS core–shell nanocrystals with narrow emission linewidths and suppressed blinking. *Nat. Mater.* **2013**, 12, 445–451.
9. Fan F. et al. Continuous-wave lasing in colloidal quantum dot solids enabled by facet-selective epitaxy. *Nature*. **2017**, 544, 75–79.
10. Iyer V. H.; Mahadevu R.; Pandey A. Low Threshold Quantum Dot Lasers. *J. Phys. Chem. Lett.* **2016**, 7, 1244–1248.
11. Grim J. Q.; Christodoulou S.; Di Stasio F.; Krahne R.; Cingolani R.; Manna L.; Moreels I. Continuous-wave biexciton lasing at room temperature using solution-processed quantum wells. *Nat. Nanotechnol.* **2014**, 9, 891–895.
12. Schmidt L. C.; Pertegás A.; González-Carrero S.; Malinkiewicz O.; Agouram, S.; Mínguez Espallargas G.; Bolink H. J.; Galian, R. E.; Pérez-Prieto J. Nontemplate Synthesis of CH<sub>3</sub>NH<sub>3</sub>PbBr<sub>3</sub> Perovskite Nanoparticles. *J. Am. Chem. Soc.* **2014**, 136, 3, 850–853.
13. Protesescu L.; Yakunin S.; Bodnarchuk M. I.; Krieg F.; Caputo R.; Hendon C. H.; Yang R. X.; Walsh A.; Kovalenko M. V. Nanocrystals of Cesium Lead Halide Perovskites (CsPbX<sub>3</sub>, X = Cl, Br, and I): Novel Optoelectronic Materials Showing Bright Emission with Wide Color Gamut. *Nano Lett.* **2015**, 15, 6, 3692–3696.
14. Protesescu L.; Yakunin S.; Bär J.; Bertolotti F.; Masciocchi N.; Guagliardi A.; Grotevent M.; Shorubalko I.; Bodnarchuk M. I.; Kumar S.; Shih C.-J.; Kovalenko M. V. Dismantling the “Red Wall” of Colloidal Perovskites: Highly Luminescent Formamidinium and Formamidinium/Cesium Lead Iodide Nanocrystals. *ACS Nano*. **2017**, 11, 3119–31134.
15. Dou L.; Wong A. B.; Yu Y.; Lai M.; Kornienko N.; Eaton S. W.; Fu A.; Bischak C. G.; Ma J.; Ding T.; Ginsberg N. S.; Wang L.-W.; Alivisatos A. P.; Yang P. Atomically thin two-dimensional organic-inorganic hybrid perovskites. *Science*. **2015**, 349, 1518–1521.
16. Sutherland B. R.; Sargent, E. H. Perovskite photonic sources. *Nat. Photonics*. **2016**, 10, 295–302.

17. Yakunin S.; Protesescu L.; Kriegn F.; Bodnarchuk M. I.; Nedelcu G.; Humer M.; De Luca G.; Fiebig, M.; Heiss W.; Kovalenko M. V. Low-threshold amplified spontaneous emission and lasing from colloidal nanocrystals of caesium lead halide perovskites. *Nat. Commun.* **2015**, 6, 8056.
18. Wang Y.; Li X.; Song J. D.; Xiao L.; Zeng H.; Sun H. All-Inorganic Colloidal Perovskite Quantum Dots: A New Class of Lasing Materials with Favorable Characteristics. *Adv. Mater.* **2015**, 27, 7101–7108.
19. Wang Y.; Li X.; Zhao X.; Xiao L.; Zeng H.; Sun H. Nonlinear Absorption and Low-Threshold Multiphoton Pumped Stimulated Emission from All-Inorganic Perovskite Nanocrystals. *Nano Lett.* **2016**, 16, 448–453.
20. Xu Y.; Chen Q.; Zhang C.; Wang R.; Wu H.; Zhang X.; Xing G.; Yu W. W.; Wang X.; Zhang Y.; Xiao M. Two-Photon-Pumped Perovskite Semiconductor Nanocrystal Lasers. *J. Am. Chem. Soc.* **2016**, 138, 3761–3768.
21. Pan J.; Sarmah S. P.; Murali B.; Dursun I.; Peng W.; Parida M. R.; Liu J.; Sinatra L.; Alyami N.; Zhao C.; Alarousu E.; Ng T. K.; Ooi B. S.; Bark O. M.; Mohamed O. F. Air-Stable Surface-Passivated Perovskite Quantum Dots for Ultra-Robust, Single- and Two-Photon-Induced Amplified Spontaneous Emission. *J. Phys. Chem. Lett.* **2015**, 6, 5027–5033.
22. Veldhui S. A.; Boix P. P.; Yantara N.; Li M.; Sum T. C.; Mathews N.; Mhaisalkar S. G. Perovskite Materials for Light-Emitting Diodes and Lasers. *Adv. Mater.* **2016**, 28, 6804–6834.
23. Zhang Q.; Su R.; Liu X.; Xing J.; Sum T. C.; Xiong, Q. High-Quality Whispering-Gallery-Mode Lasing from Cesium Lead Halide Perovskite Nanoplatelets. *Adv. Funct. Mater.* **2016**, 26, 6238–6245.
24. Park Y. S.; Guo, S.; Makarov N. S.; Klimov V. I. Light–Matter Interactions in Cesium Lead Halide Perovskite Nanowire Lasers. *J. Phys. Chem. Lett.* **2016**, 7, 3703–3710.
25. Ha S. T.; Su R.; Xing J.; Zhang Q.; Xiong, Q. Metal halide perovskite nanomaterials: synthesis and applications. *Chem. Sci.* **2017**, 8, 2522–2536.
26. Tang X.; Hu Z.; Chen W.; Xing X.; Zang Z.; Hu W.; Qiu J.; Du J.; Leng Y.; Jiang X.; Mai X. Room temperature single-photon emission and lasing for all-inorganic colloidal perovskite quantum dots. *Nano Energy*. **2016**, Vol. 28, pp. 462–468.
27. Polavarapu L.; Nickel B.; Feldmann J.; Urban A. S. Advances in Quantum-Confined Perovskite Nanocrystals for Optoelectronics. *Adv. Energy Mater.* **2017**, 5, 1500963.
28. Lin C. H.; Lafalce W.; Jung J.; Smith M. J.; Malak S. T.; Aryal S.; Yoon Y. J.; Zhai Y.; Lin Z.; Vardeny A. V.; Tsukruk V. V. Core/Alloyed-Shell Quantum Dot Robust Solid Films with High Optical Gains. *ACS Photonics*. **2016**, 3, 647–658.
29. Lhuillier E.; Pedetti S.; Ithurria S.; Nadal B.; Heuclin H.; Dubertret B. Two-dimensional colloidal metal chalcogenides semiconductors: synthesis, spectroscopy, and applications. *Acc. Chem. Res.* **2015**, 48, 22–30.
30. She C; Fedin I.; Dolzhenkov D. S.; Demortiere A.; Schaller R. D.; Pelton M.; Talapin D. V. Low-threshold stimulated emission using colloidal quantum wells. *Nano Lett.* **2014**, 14, 2772–2777 .

31. De Jong E. M. L. D.; Yamashita G.; Gomez L.; Ashida M.; Fujiwara, Y.; Gregorkiewicz T. Multiexciton Lifetime in All-Inorganic CsPbBr<sub>3</sub> Perovskite Nanocrystals. *J. Phys. Chem. C*. **2017**, 121, 1941–1947.
32. Makarov N. S.; Guo S.; Isaienko O.; Liu W.; Robel I.; Klimov V. I. Spectral and Dynamical Properties of Single Excitons, Biexcitons, and Trions in Cesium–Lead-Halide Perovskite Quantum Dots. *Nano Lett.* **2016**, 16, 2349–2362.
33. Mingjie L.; Bhaumik S.; Goh T. W.; Kumar M. S.; Yantara N.; Gratzel M.; Mhaisalkar S.; Mathews N.; Sum T. C. Slow cooling and highly efficient extraction of hot carriers in colloidal perovskite nanocrystals. *Nat. Comm.* **2017**, 8, 14350.
34. Papagiorgis P.; Protesescu L.; Kovalenko M. V.; Othonos A.; Itskos G. Long-Lived Hot Carriers in Formamidinium Lead Iodide Nanocrystals. *J. Phys. Chem. C*. **2017**, 121, 12434 – 12440
35. Chen K.; Barker A. J.; Morgan F. L. C.; Halpert J. E.; Hodgkiss J. M. Effect of Carrier Thermalization Dynamics on Light Emission and Amplification in Organometal Halide Perovskites. *J. Phys. Chem. Lett.* **2015**, 6, 153–158.
36. Manser J. S.; Christians J. A.; Kamat, P. V. Intriguing Optoelectronic Properties of Metal Halide Perovskites. *Chem. Rev.* **2016**, 116, 12956–13008
37. Berry J.; Buonassisi T.; Egger D. A.; Hodes G.; Kronik L.; Loo Y. L.; Lubomirsky I.; Mander S. R.; Astai Y.; Miller J. S.; Mitzi D. B.; Paz Y.; Rappe A. M.; Riess I.; Rybtchinski B.; Stafsudd O.; Stevanovic V. Tonney M. F.; Zitoun D.; Kahn A.; Ginley D.; Cahen D. Hybrid Organic-Inorganic Perovskites (HOIPs): Opportunities and Challenges. *Adv. Mater.* **2015**, 27, 5102–5112.
38. Zakutayev A.; Caskey C. M.; Fioretti A. N.; Ginley D. S.; Vidal J.; Stevanovic V.; Tea E.; Lany, S. Defect Tolerant Semiconductors for Solar Energy Conversion. *J. Phys. Chem. Lett.* **2014**, 5, 1117–1125.
39. Trots, D. M.; Myagkota, S. V. High-Temperature Structural Evolution of Caesium and Rubidium Triiodoplumbates. *J. Phys. Chem. Solids*. **2008**, 69, 2520-2526.
40. Stoumpos C. C.; Malliakas C. D.; Kanatzidis, M. G. Semiconducting Tin and Lead Iodide Perovskites with Organic Cations: Phase Transitions, High Mobilities, and Near-Infrared Photoluminescent Properties. *Inorg. Chem.* **2013**, 52, 9019-9038.
41. Levchuk I.; Osvet A.; Tang X.; Brandl M.; Perea J. D.; Hoegl F.; Matt G. J.; Hock R.; Batentschuk M.; Brabec C. J. Brightly Luminescent and Color-Tunable Formamidinium Lead Halide Perovskite FAPbX<sub>3</sub> (X = Cl, Br, I) Colloidal Nanocrystals. *Nano Lett.* **2017**, 17, 2765–2770.
42. Fang H. H.; Protesescu, L.; Balazs D. M.; Adjokatse S.; Kovalenko M. V.; Loi M. A. Exciton Recombination in Formamidinium Lead Triiodide: Nanocrystals versus Thin Films. *Small*. **2017**, 13, 1700673-1700682.
43. De Roo J.; Ibáñez M.; Geiregat P.; Nedelcu G.; Walravens W.; Maes J.; Martins C.; Van Driessche I.; Kovalenko V. M.; Hens Z. Highly Dynamic Ligand Binding and Light Absorption Coefficient of Cesium Lead Bromide Perovskite Nanocrystals, *ACS Nano*, **2016**, 10, 2071–2081,

44. Pan A.; HeB.; Fan X.; Liu Z.; Urban J. J.; Alivisatos A. P.; He L.; LiuY. Insight into the Ligand-Mediated Synthesis of Colloidal CsPbBr<sub>3</sub> Perovskite Nanocrystals: The Role of Organic Acid, Base, and Cesium Precursors, *ACS Nano*, 2016, 10, 7943–7954
45. Fang H. H.; Wang F.; Adjokatse S.; Zhao N.; Even J.; Loi M. A. Photoexcitation dynamics in solution-processed formamidinium lead iodide perovskite thin films for solar cell applications. *Light: Sci. & Appl.* **2016**, 5, 1-6.
46. Wright A. D.; Verdi C.; Milot R. L.; Eperon E. G.; Pe´rez-Osorio M. A.; Snaith H. J.; Giustino F.; Johnston M. B.; Herz L. M. Electron–phonon coupling in hybrid lead halide perovskites. *Nat. Comm.* **2016**, 7, 11755.
47. Eperon G. E.; Stranks S. D.; Menelaou C.; Johnston M. B.; Herz L. M.; Snaith H. J. Formamidinium lead trihalide: a broadly tunable perovskite for efficient planar heterojunction solar cells. *Energy Environ. Sci.* **2014**, 7, 982-988.
48. Jacobsson J. T.; Correa-Baena J.-P.; Anaraki H. E.; Philippe B.; Stranks D. S.; Bouduban E. F. M.; Tress W.; Schenk K.; Teuscher J.; Moser E. J.; RensmoH.; Hagfeldt A.; Unreacted PbI<sub>2</sub> as a Double-Edged Sword for Enhancing the Performance of Perovskite Solar Cells, *J. Am. Chem. Soc.*, **2016**, 138, 10331–10343
49. Stadler P.; Mohamed S. A.; Gasiorowski J.; Sytnyk M.; Yakunin S.; Scharber M. C.; Enengl C.; Enengl S.; Egbe D. A. M.; El-Mansy M. K.; Obayya S. S. A.; Sariciftci N. S.; Hingerl K.; Heiss W. Iodide-Capped PbS Quantum Dots: Full Optical Characterization of a Versatile Absorber. *Adv. Mater.* **2015**, 27, 1533–1539.
50. Yuan F.; Wu Z.; Dong H.; Xi J.; Xi K.; Divitini G.; Jiao B.; Hou .; Wang S.; Gong Q. High Stability and Ultralow Threshold Amplified Spontaneous Emission from Formamidinium Lead Halide Perovskites Films. *J. Phys. Chem. C* **2017**, 121, 15318–15325.
51. Shaklee K. L.; Leheny, R. F. Direct determination of optical gain in semiconductor crystals. *Appl. Phys. Lett.* **1971**, 18, 475–477 .
52. Casperson L. W.; Yariv A. Spectral Narrowing in High-Gain Lasers. *IEEE J. Quantum Electron.* **1972**, 8, 80-85.
53. de Mello, J. C.; Wittmann, H. F.; Friend, R. H. An Improved Experimental Determination of External Photoluminescence Quantum Efficiency. *Adv. Mater.* **1997**, 9, 230–232.

**TOC Graphic**

